Liu, Y., Zhao, G., Terziev, M., Dai, D., Feng, A., & Yuan, Z. (2024). Unsteady hydrodynamics of a surface piercing and fully submerged body when entering a lock. Physics of Fluids, 36, Article 063111. https://doi.org/10.1063/5.0211552

Unsteady hydrodynamics of a surface piercing and fully submerged body when entering a lock

Yihan Liu[1], Guangwei Zhao[1], Momchil Terziev[1], Saishuai Dai[1],
Aichun Feng[2], Zhi-Ming Yuan[1*]

[1]Department of Naval Architecture, Ocean and Marine Engineering,
University of Strathclyde, Glasgow, G4 0LZ, United Kingdom.
[2]School of Naval Architecture, Ocean and Civil Engineering, Shanghai
Jiao Tong University, Shanghai, 200240, China.

*Corresponding author(s). E-mail(s): zhiming.yuan@strath.ac.uk;

Abstract

Ship hydrodynamics in a constant waterway have been well studied. With a coordinate system fixed on the moving ship, the boundary value problem (BVP) is usually treated as a steady one. However, the hydrodynamics of a ship moving in confined waterways with abrupt changes in width or depth are complex due to their unsteady nature. The studies on such unsteady problems are insufficient. In the engineering practise, the hydrodynamic unsteadiness can be fully reflected by a scenario when a ship enters a lock. Prior studies have predominantly focused on predicting the ships' hydrodynamic forces without considering the unsteady terms on the free-surface boundary conditions. Obviously, such steady or quasi-steady methods overlooked the crucial unsteady phenomenons on free water surface. To address this gap, the present study introduces a novel three-level difference scheme to discretize the free surface condition, preserving unsteady terms while maintaining temporal continuity of cells on the free surface. With the implementation of such fully unsteady BVP, we observed some interesting unsteady free surface motions which were not well documented in the existing literature. To verify our new observations, as well as to validate the numerical method proposed in this study, two physical model tests were designed and conducted in a towing tank: a submerged ellipsoid enters into a deep lock at relatively high speeds, and a box enters into a shallow and narrow lock at very low speeds. The discussions are highlighted on the unsteady waves in front of the moving bodies, as well as the unsteady resistance induced by such waves.

Keywords: potential flow theory, hydrodynamics, unsteady effect, ship-lock problem

1 Introduction

The maneuverability of ships during entry into a lock remains inadequately understood due to the intricate hydrodynamic interactions involved. Various factors, including approach channel and structure layouts, water depth variations, translation waves, return flow, and cushion effects, contribute to the changing hydrodynamic characteristics encountered by ships entering a lock[1]. This assertion finds support in real-world operations where ships experience abrupt reductions in channel width and depth upon entering a lock. Consequently, the flow is compressed around the ship's bottom and sides, leading to increased flow velocity and reduced pressure on the ship. Analysis of pressure distribution indicates an inclination for the ship to move towards the lock bottom. Simultaneously, the pressure disparity between the bow and stern induces wave making resistance and pitch moments. Consequently, a decrease in water depth amplifies wave making resistance, sinkage, and trim values. Moreover, asymmetrical waterway shapes on the ship's port and starboard sides introduce lateral forces and yaw moments, potentially causing the ship to skew towards the bank. These phenomena pose inherent risks to ships entering locks, including grounding and collision incidents. Notably, the blockage of the Suez Canal in March 2021 resulted from a cargo ship becoming stranded in the waterway.

Over recent decades, researchers have invested substantial efforts in exploring the hydrodynamic behaviors of ships navigating through constrained waterways. As noted previously, ships approaching locks undergo notable behavioral transformations due to deceleration, shallow-water effects, and interactions with banks and other vessels. Consequently, a considerable body of research has focused on examining ship-bank effects experienced by ships operating in shallow waters. The David Taylor Model Basin conducted numerous experiments to investigate variations in ship maneuverability in the Panama Canal across different cross-sections[2]. Norrbin conducted extensive experimental and analytical studies on bank effects[3]. Additionally, Flanders Hydraulics Research and Ghent University conducted a series of model tests examining ship-bank[4][5], ship-bottom[6][5], ship-lock[7], and ship-ship interactions[8]. These investigations indicate that a sailing ship's hydrodynamic behavior in narrow channels is significantly influenced by both vertical and horizontal boundaries.

Moreover, researchers have directed attention towards the velocity of ships entering locks and the resultant waves generated within the locks. Vrijburcht computed the wave height and corresponding ship speed during lock entry[9]. Meng et al. conducted simulations to elucidate the intricate flow patterns generated by ships entering locks at varying speeds[10]. Their study revealed the accumulation of water ahead of the ship during lock entry. Wan et al. focused on the wave phenomena induced by ships entering locks[11]. Their investigation centred on a typical branched lower approach channel system, examining water-level fluctuations in response to discharge, interval running time, and the location of emptying outlets during lock operations.

However, existing research has predominantly focused on the hydrodynamic effects of ships entering locks and the fluctuations in wave height or water level within the locks. Nonetheless, there has been limited exploration into the intricate wave phenomena generated during the ship entry process into locks. Therefore, the principal objective of this paper is to delve into these wave phenomena. To achieve this goal, the existing potential flow solver MHydro, based on a 3D boundary element method (BEM) utilising a Rankine source function[12], is enhanced and refined. This refinement aims to simulate unsteady wave fields within locks and predict ship hydrodynamic performance in confined waterways. The subsequent sections will introduce the detailed mathematical modelling and numerical simulation setup of MHydro in Chapter 2. Following that, Chapter 3 will focus on investigating wave phenomena occurring during lock entry, with two most probable scenarios selected for analysis: one involving an ellipse entering the lock, and the other a box entering the lock. Finally, Chapter 4 presents the conclusions drawn from this study.

2 Mathematical modelling

2.1 Boundary value problem

As depicted in Figure 1, this study employs two distinct right-hand coordinate systems: a global coordinate system $O-XYZ$, fixed to the midpoint of the lock entrance, and a local coordinate system $o_0-x_0y_0z_0$, positioned at the geometric center of the ship.

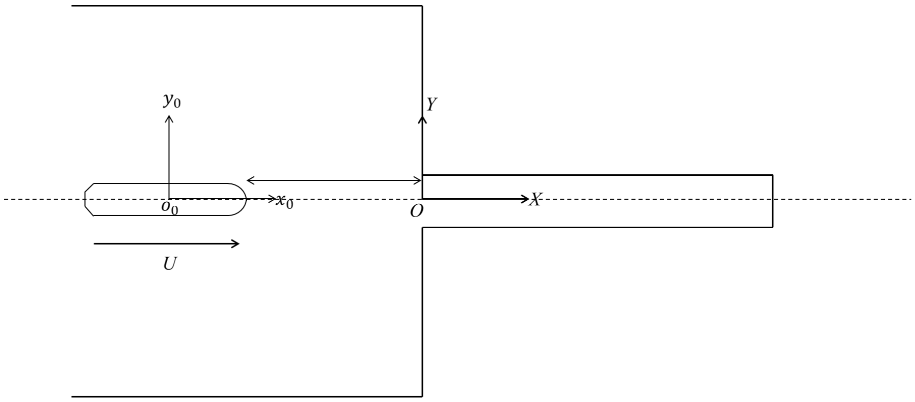

Fig. 1: Sketch of the problem

In the global coordinate system, the positive direction of the x-axis extends from the lock entrance towards the lock gate. Conversely, in the local coordinate system, the x-axis extends from the ship's stern to its bow, while both z-axes have an upward positive direction. The ship moves at a constant velocity U along the positive x-axis direction as it gradually enters the ship lock. It is crucial to note that, due to the reliance on potential flow theory, the fluid in this study is considered ideal, meaning it is assumed to be inviscid, irrotational, and incompressible. Flow is described using a velocity potential $\phi(x, y, z, t)$, while the free surface is represented by the wave elevation $\zeta(x, y, t)$.

The velocity potential $\phi(x, y, z, t)$ satisfies the Laplace equation:

$$\frac{\partial^2\varphi}{\partial x^2}+\frac{\partial^2\varphi}{\partial y^2}+\frac{\partial^2\varphi}{\partial z^2}=0 \tag{1}$$

The free surface is expressed by the kinematics and dynamics free surface conditions:

$$\frac{\partial\zeta}{\partial t}-U\frac{\partial\zeta}{\partial x}+\frac{\partial\varphi}{\partial x}\frac{\partial\zeta}{\partial x}+\frac{\partial\varphi}{\partial y}\frac{\partial\zeta}{\partial y}-\frac{\partial\varphi}{\partial z}=0,\ \text{at } z=\zeta \tag{2}$$

$$\frac{\partial\varphi_u}{\partial t}-U\frac{\partial\varphi}{\partial x}+g\zeta+\frac{1}{2}\nabla\varphi\cdot\nabla\varphi+\frac{P}{\rho}=0,\ \text{at } z=\zeta \tag{3}$$

where g is the acceleration of gravity, ρ is the fluid density and P is the forcing pressure on the free surface. φ_t and ζ_t are the time derivative of φ and ζ. φ_x, φ_y and φ_z are the x, y, and z-direction derivatives of φ, respectively.

In this paper, it is important to note that the neglect of nonlinear terms on free surface conditions implies an inability to quantify the influence of nonlinear effects on unsteady phenomena. However, drawing upon published research, some pertinent conclusions can still be inferred. Specifically, when a ship experiences sustained acceleration in shallow water, the wave resistance it encounters can be accurately predicted by both the linear and unsteady potential flow solver MHydro and Computational Fluid Dynamics (CFD) methods. Notably, predictions from both approaches exhibit close agreement, with only minor discrepancies evident near critical speeds[13]. This observation underscores the dominance of unsteady effects in wave making resistance when a ship navigates at low speeds in shallow water and the influence of nonlinear effects remains relatively limited.

Then the free surface conditions are discretized by inducing and extending the numerical programme MHydro[12][14]. Specifically, a kind of three-level scheme is used to obtain the derivatives of φ and ζ in time and location scale:

$$\begin{aligned}(\varphi_t)_{i,j}^{m+1}&=\frac{1}{\Delta t}\left(\frac{3}{2}\varphi_{i,j}^{m+1}-2\varphi_{i,j}^{m}+\frac{1}{2}\varphi_{i,j}^{m-1}\right)\\(\zeta_t)_{i,j}^{m+1}&=\frac{1}{\Delta t}\left(\frac{3}{2}\zeta_{i,j}^{m+1}-2\zeta_{i,j}^{m}+\frac{1}{2}\zeta_{i,j}^{m-1}\right)\end{aligned} \tag{4}$$

$$\begin{aligned}(\varphi_x)_{i,j}^{m+1}&=\frac{1}{\Delta x}\left(\frac{3}{2}\varphi_{i,j}^{m+1}-2\varphi_{i,j+1}^{m+1}+\frac{1}{2}\varphi_{i,j+2}^{m+1}\right)\\(\zeta_x)_{i,j}^{m+1}&=\frac{1}{\Delta x}\left(\frac{3}{2}\zeta_{i,j}^{m+1}-2\zeta_{i,j+1}^{m+1}+\frac{1}{2}\zeta_{i,j+2}^{m+1}\right)\end{aligned} \tag{5}$$

where m represents the n-th time step and i and j indicate that the element is located on the i-th row and j-th column on the free surface. As a result, the kinematic free surface condition can be discretized firstly at iterative step k as:

$$\begin{aligned}&\frac{1}{\Delta t}\left(\frac{3}{2}\zeta_{i,j}^{(m+1,k)}-2\zeta_{i,j}^{(m,k)}+\frac{1}{2}\zeta_{i,j}^{(m-1,k)}\right)\\&-U\frac{1}{\Delta x}\left(\frac{3}{2}\zeta_{i,j}^{(m+1,k)}-2\zeta_{i,j+1}^{(m+1,k)}+\frac{1}{2}\zeta_{i,j+2}^{(m+1,k)}\right)-\frac{\partial\varphi_{i,j}^{(m+1,k)}}{\partial z}=0\end{aligned} \tag{6}$$

$$\begin{aligned}&\frac{3}{2}\left(\frac{1}{\Delta t}-\frac{U}{\Delta x}\right)\zeta_{i,j}^{(m+1,k)}+2\frac{U}{\Delta x}\zeta_{i,j+1}^{(m+1,k)}-\frac{1}{2}\frac{U}{\Delta x}\zeta_{i,j+2}^{(m+1,k)}\\&=\frac{2}{\Delta t}\zeta_{i,j}^{(m,k)}-\frac{1}{2}\frac{1}{\Delta t}\zeta_{i,j}^{(m-1,k)}+\frac{\partial\varphi_{i,j}^{(m+1,k)}}{\partial z}\end{aligned}\tag{7}$$

Then the value of $\zeta_{i,j}^{m+1}$ is obtained accordingly and updating the value of unknown potential φ at t_{m+1} also becomes feasible now:

$$\begin{aligned}&\frac{1}{\Delta t}\left(\frac{3}{2}\varphi_{i,j}^{(m+1,k)}-2\varphi_{i,j}^{(m,k)}+\frac{1}{2}\varphi_{i,j}^{(m-1,k)}\right)\\&-U\frac{\partial\varphi_{i,j}^{(m+1,k)}}{\partial x}+g\zeta_{i,j}^{(m+1,k)}=0\end{aligned}\tag{8}$$

$$\begin{aligned}&\frac{3}{2}\frac{1}{\Delta t}\varphi_{i,j}^{(m+1,k)}-U\frac{\partial\varphi_{i,j}^{(m+1,k)}}{\partial x}\\&=\frac{2}{\Delta t}\varphi_{i,j}^{(m,k)}-\frac{1}{2}\frac{1}{\Delta t}\varphi_{i,j}^{(m-1,k)}-g\zeta_{i,j}^{(m+1,k)}\end{aligned}\tag{9}$$

After the above calculation, $\varphi_{i,j}^{(m,k)}$ and $\zeta_{i,j}^{(m,k)}$ are predicted as the new value of $\varphi_{i,j}^{m}$ and $\zeta_{i,j}^{m}$. In order to generate a stable result, these new values must satisfy both conditions of $\left|\varphi_{i,j}^{(m,k)}-\varphi_{i,j}^{(m,k-1)}\right|<\varepsilon$ and $\left|\zeta_{i,j}^{(m,k)}-\zeta_{i,j}^{(m,k-1)}\right|<\varepsilon$ before proceeding to the next time step.

Apart from the free surface conditions, the boundary conditions on body should reflect the body surface is impenetrable and the value of the flow's normal velocity should be the same as the ship velocity U:

$$\frac{\partial\varphi}{\partial\boldsymbol{n}}=Un_1\tag{10}$$

where $\boldsymbol{n}=(n_1,n_2,n_3)$ is the unit normal vector on body surface while normal direction is pointing from the body surface to the fluid domain.

On the sea bottom and side walls, the same boundary condition with the body surface is applied, but the normal velocity of flow here should equal to zero:

$$\frac{\partial\varphi}{\partial\boldsymbol{n}}=0\tag{11}$$

After the unknown potential φ has been solved, the forces/moments can be obtained from the Bernoulli's equation

$$F_i=\iint_S pn_i\ \mathrm{d}S, i=1,2,\cdots,6\tag{12}$$

where

$$p = -\rho \left[\frac{\partial \varphi}{\partial t} - U \frac{\partial \varphi}{\partial x} + \frac{1}{2} (\nabla \varphi)^2 \right] \tag{13}$$

Similarly, the free surface elevation can be expressed as:

$$\zeta(x, y, t) = -\frac{1}{g} \left[\frac{\partial \varphi}{\partial t} - U \frac{\partial \varphi}{\partial x} + \frac{1}{2} (\nabla \varphi)^2 \right] \tag{14}$$

2.2 Numerical simulation set-up

In the numerical modelling, panels are exclusively distributed on the body surface, free surface, and bank surface. For the bottom surface, to expedite computation time, it was not explicitly modelled in the simulation. Instead, mirroring techniques were employed to treat it as a mirror, accounting for its influence on the computational results. Similarly, this study leverages the symmetry of the calculation domain and only models half of the domain.

Additionally, through testing, this study chose to truncate the computational domain four ship lengths aft of the ship's stern. At this juncture, the domain boundary does not impact the simulation results. Furthermore, as previously mentioned, the free surface remains continuous in the time domain, moving forward with the ship to maintain a constant distance between the panels on the free surface and the ship hull throughout the simulation.

The wave making resistance in this study has been non-dimensionalised, denoted by the wave making resistance coefficient:

$$C_w = \frac{R_w}{(1/2)\rho U^2 S} \tag{15}$$

In Eq. (15), S is the area of the wet body surface, ρ is the density of the water, U is the velocity of the ellipsoid and R_w denotes the wave making resistance, which equals F_1 in Eq. (12).

Furthermore, a convergence analysis is also included in this study to ensure the stability of the numerical simulation results, as shown in Figure 2:

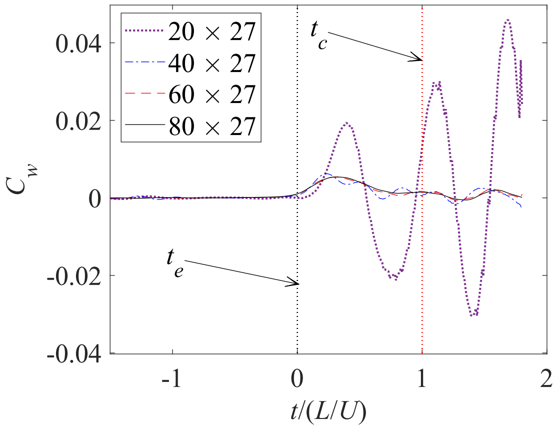

Fig. 2: Convergence study on the numerical model where C_w is the wave making resistance coefficient of the ellipsoid and $t/(L/U)$ is the dimensionless over time t

The convergence study of the number of panels on the free surface includes four sets of grids, i.e., 40×27, 60×27 and 80×27 panels in the x and y directions within each ship length. It is observable that when the density of mesh is relatively sparse, the predicted wave making resistance exhibits considerable volatility, with the resistance curve not being smooth. However, as the density increases, these issues are noticeably ameliorated. After considering both the accuracy of the computational results and computational efficiency, this study uses the third set of grids to construct the numerical model.

At the same time, due to the use of a completely unsteady method in the present study, it is necessary to ensure that all results are interrelated to each other at each time step, while this method also has strict requirements on the time step. In the end, the time step in this simulation was set to 0.0139s.

3 Results and discussions

This study delves into hydrodynamic phenomena encountered as objects navigate narrow water passages, focusing on two distinct cases. The first involves a submerged ellipsoid entering a lock at relatively high speed in deep water. Conversely, the second case, more representative of practical scenarios, entails a box navigating into the lock under shallow and narrow water conditions at a lower speed. This chapter will further elaborate on these cases in two sections and explore their interrelation in the summary section.

3.1 A submerged ellipsoid entering a lock in deep water at medium speed

As previously mentioned, the first case investigated in this study involves a submerged ellipsoid entering a lock at a moderate speed in deep water. In this scenario, since the cross-sectional area of the ellipsoid is significantly smaller compared to the cross-sectional area of the lock, the wave field inside the lock primarily arises from changes in the velocity of the ellipsoid, rather than alterations in the volume of water.

3.1.1 Experimental set-up

The experiment involving the ellipsoid was conducted in the 3D Compact Wave Tank (Figure 3) situated within the Kelvin Hydrodynamics Laboratory at the University of Strathclyde. This tank measures 9.27 meters in length, 3.15 meters in width, and maintains a fixed water depth of 1.00 meter. The ellipsoid model, fabricated from Divinycell foam, was equipped with internal ballast weights to attain a naturally buoyant condition (see Figure 4).

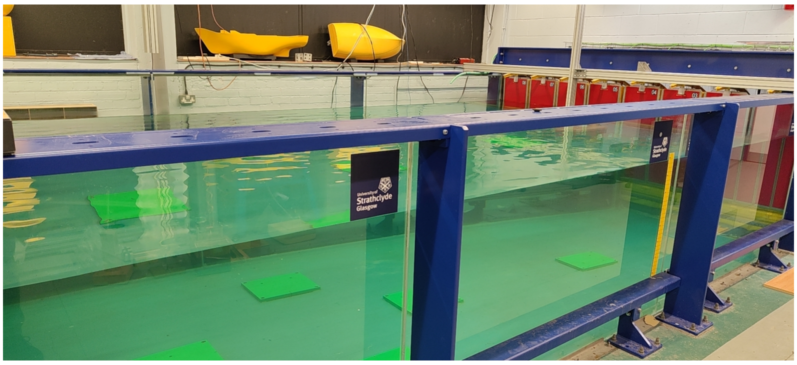

Fig. 3: 3D Compact Wave Tank in Kelvin Hydrodynamics Laboratory

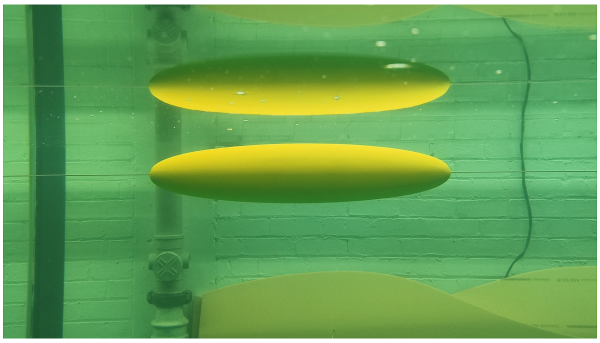

Fig. 4: Ellipsoid Model: Neutral Buoyancy in Water

The experimental setup is similar to what was adopted in the study done by Kozin[15]. In order to build such a towing system, there is an Aluminium extrusion fixed perpendicularly to the water surface at each end of the tank. Each extrusion was equipped with two pulleys (see Figure 5), one submerged underwater and the other positioned above the water surface. A stepper motor was fixed on one of the extrusions, approximately 300 mm from the top. Attached to the motor shaft was a 10.00 mm diameter collar. A thin fishing line (0.40 mm in diameter) was wound around this collar and fed through the four pulleys, connecting two ends of the model to form a closed loop. The fishing line was pre-tensioned to ensure it remained taut, limiting the lateral motions of the model as much as possible. Additionally, the tension ensured that the friction between the fishing line and the collar could drive the model at set velocities without snitching. In addition, a stainless steel wire was secured to the two vertical extrusions, passing through the ellipsoid model (Figure 5). The wire was also tensioned to maintain a taut state. Therefore the ellipsoid was able to slide only along the wire in the tank length direction.

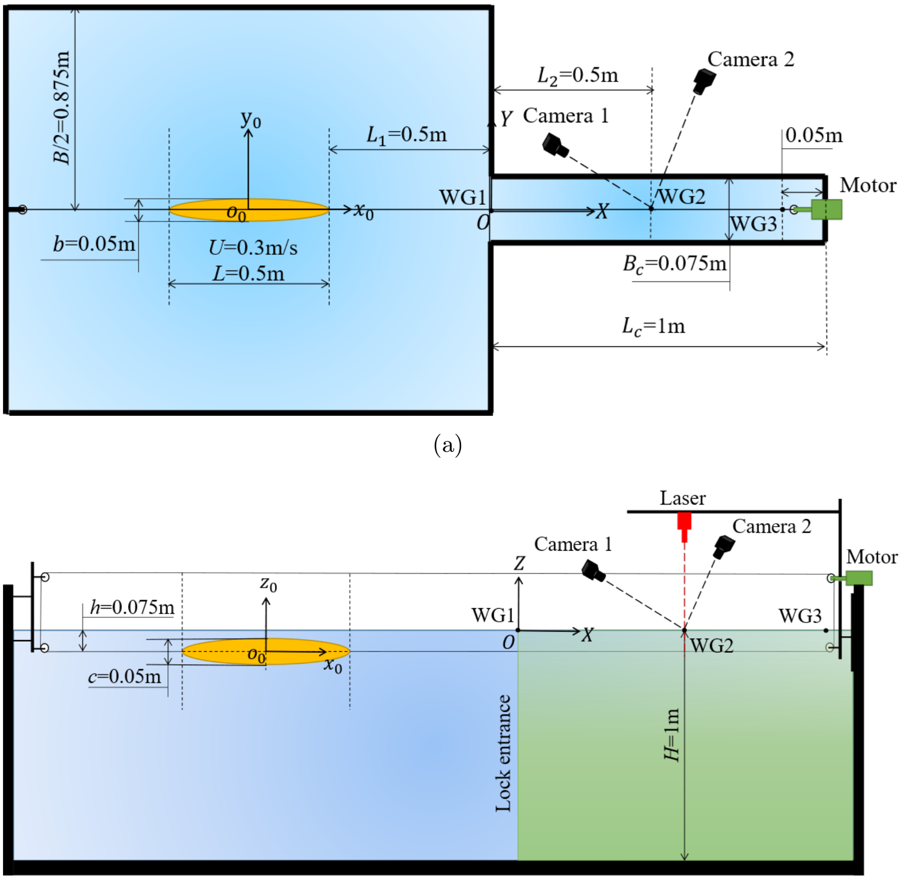

(a)

(b)

Fig. 5: The sketch of the problem and the experimental setup: (a) top view; (b) side view

The lock model was constructed using Marine Plywood. Aluminium extrusions were fitted to the back side of the lock model to strengthen the model and secure the lock into positions, as shown in Figure 6. The width of the lock area was 1.5 times the width of the ellipsoid, measuring 150 mm, while the length was 1000 mm, twice the length of the ellipsoid. Due to the limited space between the ellipsoid and the lock when the model enters the lock, instead of using intrusive resistance-type wave gauges to measure wave elevations inside the lock, an optical method based on the stereo vision principle was used: A steady-state low-power laser transmitter was used to provide a visual tracking target, by projecting a laser dot at a desired water surface area. Two Z Cam E2 movie cameras set above the lock continuously record the projected laser dot at 4k resolution and 60Hz frame rate. Thus, the time-history information of the free surface elevation at this point is obtained by calculating the spatial information of the laser dot.

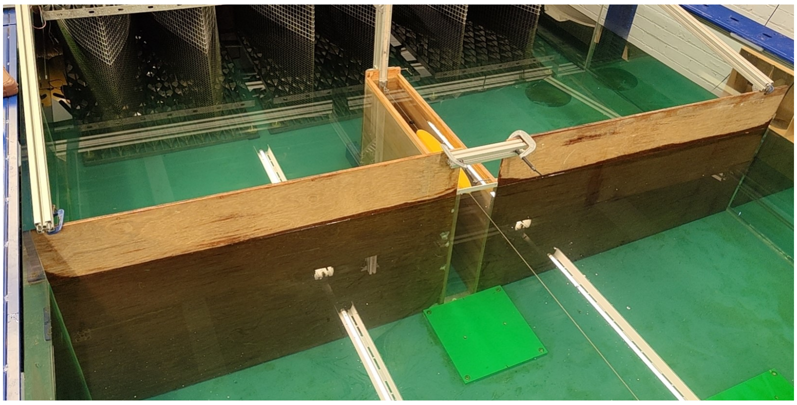

Fig. 6: Ellipsoid inside the lock area

3.1.2 Validations and discussions of the numerical simulation

Figure 7 illustrates the specific mesh arrangement employed in the simulation of this case:

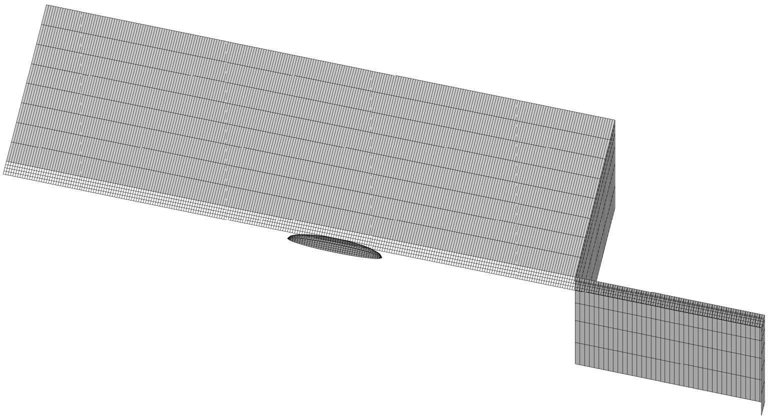

Fig. 7: Panel distribution on the computation domain of an ellipsoid advancing into a lock, there are 600, 468 and 4440 panels respectively distributed on the body, bank and free surfaces

In addition to the model experiments were conducted at KHL, the present paper also draws on Unsteady Reynolds Averaged Navier-Stokes (URANS) based Computational Fluid Dynamics (CFD) for validation. The CFD solutions are produced using the commercially available solver Star-CCM+. The developed model makes use of the Wilcox $k - \omega$ turbulence model with second order convective accuracy following previous experience which indicates computational efficiency and accuracy with this model[16]. The near-wall mesh is determined a priori using the approach detailed in with a $y^+ < 1$ in all cases[17]. The free surface is resolved using the Volume of Fluid method and since the time is discretised using a second order accurate scheme, the Courant number is limited to 0.5. This determines the time step which is set to ensure the Courant number is 0.3 to accommodate local flow acceleration. The body is encased in an overset mesh and translated in the x direction only. The results simultaneously include both pressure resistance and frictional resistance.

The computational boundaries are arranged to mirror the towing tank experiment as much as possible: the domain sides and bottom are no-slip walls. The domain top is placed one body length vertically from the undisturbed free surface which is assigned a symmetry boundary condition, in addition to the plane coincident with the domain and body midplane. A pressure outlet boundary is placed approximately to match the experiment. The mesh on the free surface is progressively refined until 15 cells per transverse wavelength ($\lambda = 2\pi U^2/g$) are achieved.

During the simulation, STAR-CCM took approximately 30,000 CPU hours, whereas MHydro, significantly faster, required only a few real hours. This substantial reduction in simulation time greatly improves the efficiency.

Results validation

Firstly, a validation is conducted by comparing the numerical results with the experimental measurements. The wave data from two fixed points in the global coordinate system were recorded in the experiment. As depicted in Figure 8, the free surface elevations at two wave gauges are captured by both numerical (MHydro and CFD) and experimental (EFD) methods. It is evident that the agreement among these three methods is generally satisfactory. Some oscillations are captured by the measurements before the ellipsoid enters the lock ($t/(L/U) < 0$), while they are not observed in the simulation results. A reasonable explanation is that these oscillations are initiated during the acceleration stage, while in the numerical simulations, a constant speed U is applied at the first time step of the simulation. The significant reduction in the oscillations observed at WG2 can support this assumption, as the accelerating waves continuously dissipate as they propagate forward. In addition to the oscillations prior to the initiation of the ellipsoid's entry into the lock, minor oscillations are also observed during the entering process. The underlying cause of this phenomenon will be elaborated upon in detail subsequently in Figure 8. It is also noted that the numerical predictions at WG2 in Figure 8 are less satisfactory, particularly when the ellipsoid gradually enters the lock. This indicates that some nonlinear phenomena may occur when the gap between the ellipsoid and the lock entrance is very small, while the method employed in this study is linear and unsteady, leading to deviations between the MHydro results and those obtained from CFD simulations and experiments.

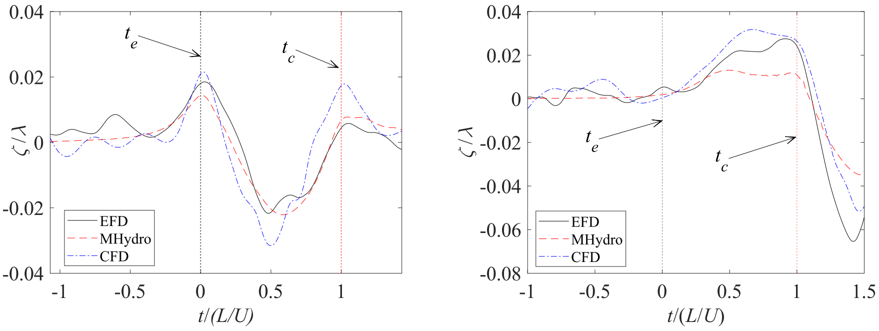

(a)

(b)

Fig. 8: Validation of free-surface elevations at Fr=0.136 where λ is the wave length of the generated wave by the ellipsoid and x axis represents the position of the ellipsoid bow under the global coordinate system: (a) free-surface elevation at WG1; (b) free-surface elevation at WG2

Piston phenomenon

Figure 9 illustrates the variation trend of the free surface inside the lock after the ellipsoid begins to enter. In this study, the water in the ship lock can be likened to a sponge, and the entry of the ellipsoid compresses the ”sponge,” causing a rise in the overall free surface. From an energy perspective, during the entry process, the water ”sponge” absorbs a portion of the ellipsoid’s kinetic energy and converts it into gravitational potential energy, resulting in the rise of the free surface. However, water is not an actual sponge; it possesses fluidity. When the free surface rises to a certain height, the accumulated potential energy is released, causing return flow within the channel and lowering the elevation of the free surface. In this study, this motion is regarded as the piston effect. The movement of the ”piston” within the gap represents an energy conversion process, so on a microscopic level, the water inside the lock can be visualized as numerous vertical slices being horizontally divided. Each slice can be considered as a spring, with the restoring force decreasing as it approaches the gate. Consequently, the amplitude of the free surface fluctuations also diminishes accordingly.

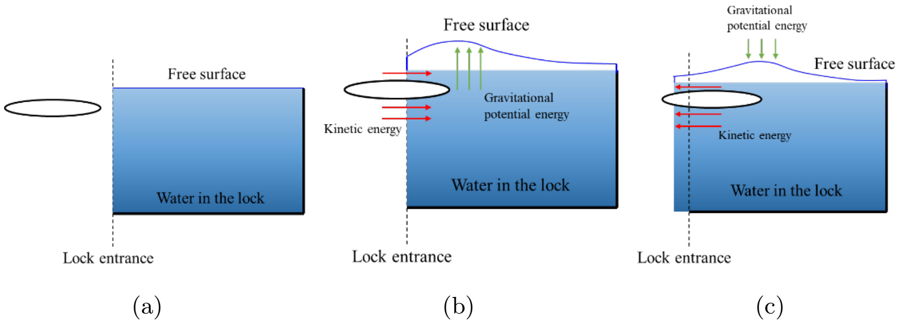

Fig. 9: The schematic diagram of the variation of the free surface inside the lock during the ellipsoid entering the lock: (a) the free surface is not disturbed; (b) the free surface rises to the highest level; (c) the free surface begins to fall

These observations are corroborated in Figure 10. Figure 10a depicts the evolution of waves along the centerline of the lock. The x-axis represents the centerline of the lock at specific moments, the y-axis denotes the temporal progress of the ellipsoid entering the lock, and the z-axis records the wave profile at each point on the centerline at the corresponding moment. For instance, t_e, t_c, and t_d respectively represent the moments when the ellipsoid has just arrived at the entrance of the lock, is fully within the lock, and is about to reach the lock gate. Consequently, the three lines in Figure 10a represent the wave profiles on the centerline of the lock at these corresponding moments. It is apparent that the free surface in the lock remains calm before t_e. However, as soon as the ellipsoid arrives at the lock entrance, waves within the lock are rapidly generated. As the ellipsoid gradually enters the lock, the free surface inside begins to undulate, as evidenced by the wave elevation at Wave Gauge 3 (WG3). WG3 records the time history of waves at the end of the lock. Both the data from WG3 and the wave elevation at the ellipsoid's bow in the body-fixed coordinate system are illustrated in Figure 10b. A distinct wave phenomenon is observable at WG3 after the initiation of entry. This phenomenon is also evident at the ellipsoid's bow.

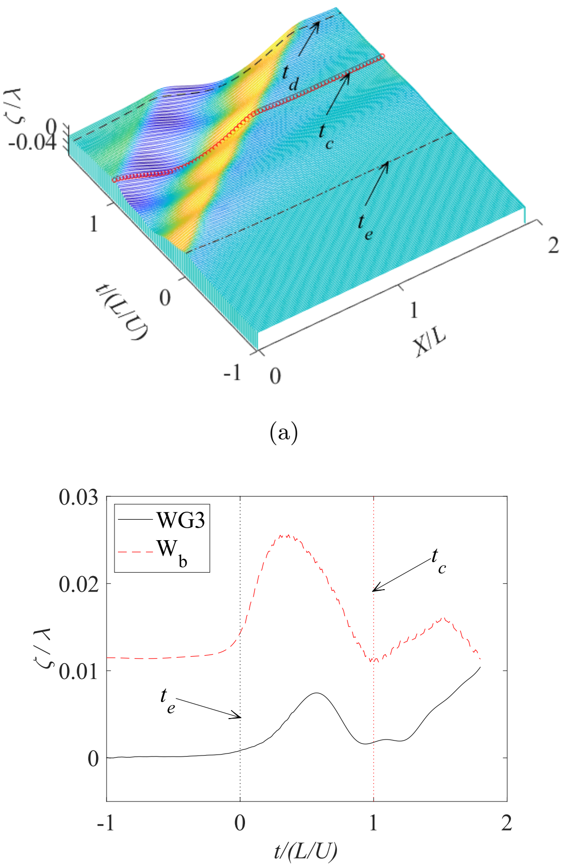

(a)

(b)

Fig. 10: Waves evolution during the ellipsoid entering the lock at Fr=0.136: (a) waterfall plot of wave cut in the centre line of lock; (b) free-surface elevation at WG3 and the ellipsoid bow

Obviously, the piston motion in the lock is affected by the entering speed. To better study the piston, a case with F_r=0.2 has been simulated. The wave elevations at five points depicted in Figure 11 are recorded, with precise coordinates provided in Table 1.

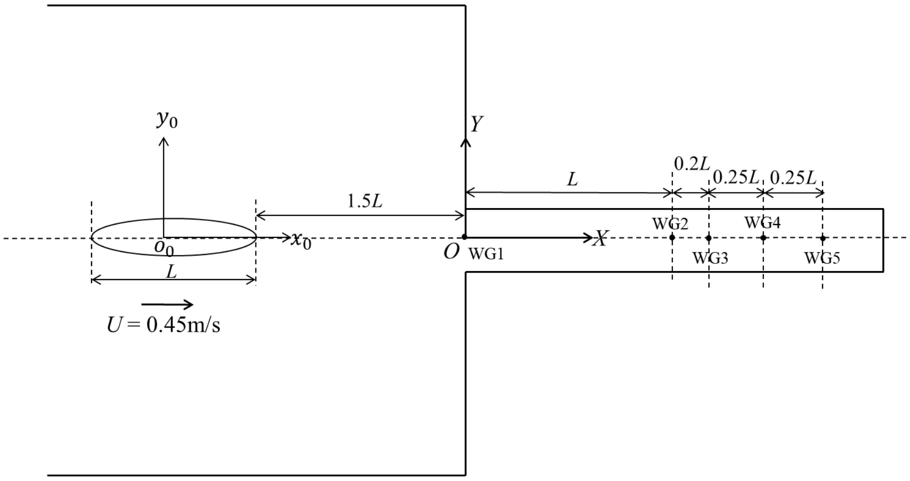

Fig. 11: The positions of wave gauges

Table 1: The positions of wave gauges in the global coordinate system

	$\boldsymbol{X(m)}$	$\boldsymbol{Y(m)}$	$\boldsymbol{Z(m)}$
WG1	0	0	0
WG2	0.5	0	0
WG3	0.6	0	0
WG4	0.725	0	0
WG5	0.85	0	0

Figure 12 illustrates the wave profiles in the lock when F_r=0.2. It is evident that the entry of the ellipsoid induces waves in the lock. A more detailed depiction of the piston motion within the lock is presented by the wave data at WG3, WG4, and WG5 in Figure 12b. After the entry of the ellipsoid ($t/(L/U) > 0$), the free surface at these three points begins to rise simultaneously. This rise reaches its peak when approximately half of the ellipsoid has entered the lock ($t/(L/U) = 0.5$), after which a decrease is observed. Due to the piston effect, a low-pressure field is established in the lock, leading to the formation of a wave trough on the free surface after $t/(L/U) > 1$. Subsequently, as the ellipsoid gradually approaches these points, the free surface at these locations is no longer influenced by the piston effect, but rather by the local pressure disturbance at the ellipsoid bow, thereby losing the characteristics of piston motions. However, the piston motion is not only evident at points near the end of the lock but can also be observed at the entrance of the lock.

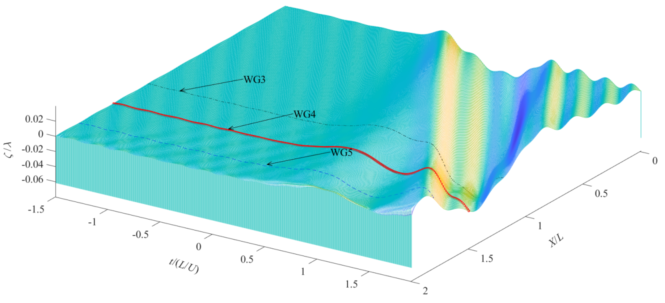

(a)

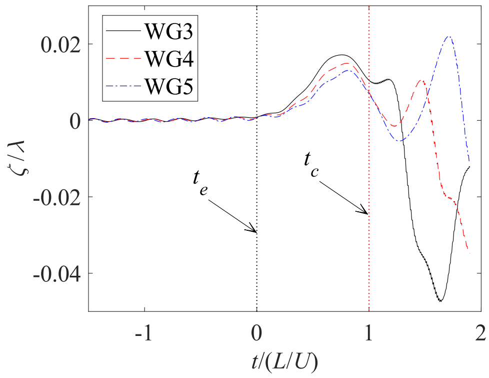

(b)

Fig. 12: Wave cuts in the lock: (a) waves evolution in the centre line of lock during the ellipsoid entering the lock when Fr=0.2; (b) free surface elevation at WG3, WG4 and WG5

However, it should be noted that the phenomenon of the free surface rising and falling simultaneously is not entirely synchronous. While the elevation changes of the free surface inside the lock are indeed a result of the piston effect, they are also influenced by variations in the pressure field caused by the forward motion of the ellipsoid. In fact, this study observes a slight time difference in the changes of the free surface at the three points depicted in Figure 12b. This difference is only evident because these three points are relatively close to each other, and the piston effect dominates at this time, making the discrepancy less noticeable.

Additionally, the waves at WG1, WG2, and WG5 are also influenced by the piston effect. As shown in Figure 13a, due to its location at the entrance of the lock, the waves at WG1 are mainly dominated by the pressure field around the ellipsoid, resulting in different characteristics compared to other locations. However, even with such positioning, the piston effect is still evident. It can be observed from Figure 13a that the wave elevation at WG1 reaches its trough when approximately half of the ellipsoid has entered the lock ($t/(L/U) = 0.5$). Thereafter, as shown in Figure 13b, a rise is expected due to the high-pressure field located at the stern of the ellipsoid approaching the lock entrance. Interestingly, after a brief increase, the wave elevation at WG1 exhibits a decreasing trend again, which occurs almost simultaneously with the decrease in wave elevation at WG2 and WG5. It may be postulated that this is because at this moment, the rise of the free surface inside the lock reaches its peak and begins to release stored gravitational potential energy, leading to the decrease at WG1. However, due to the presence of the high-pressure field at the ellipsoid stern, this decrease is very short-lived, so the wave elevation at WG1 quickly resumes its rapid upward trend. In conclusion, the phenomenon observed at WG1 is also caused by the piston effect.

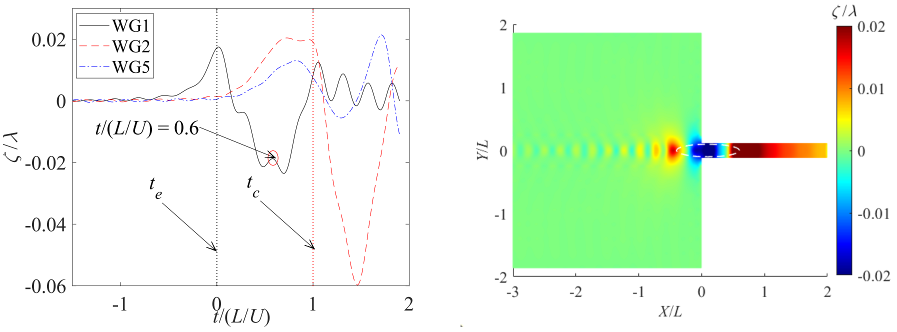

(a)

(b)

Fig. 13: Wave cuts in the lock: (a) free surface elevation at WG1, WG2 and WG5; (b) Wave field when $t/(L/U) = 0.6$

The causes of the piston phenomenon

Since this study considers that the piston effect is caused by the combination of the unsteady effect due to the sudden narrowing of the waterway and the obstruction of water by the closed lock gate, a steady case and a case with an open lock gate were simulated to prove this hypothesis. As shown in Figure 14a, the wave elevations at WG3, WG4, and WG5 are recorded to observe the fluctuation of the free surface inside the lock. It can be seen from Figure 14 that in the steady case, except for slight fluctuations, the free surface at WG3, WG4, and WG5 remains calm between $t/(L/U) > 0$ and $t/(L/U) < 1$. Notably, noticeable wave elevations are observed only when the ellipsoid gradually approaches these positions. Clearly, in the steady case, the wave elevations at the selected points are completely dominated by the local pressure field around the ellipsoid, and there is no evidence of piston motion. Therefore, it can be explicitly stated in this study that the piston effect is inseparable from the unsteady wave generated when the ellipsoid enters the lock.

However, the results in Figure 14b seem to lead to some different conclusions. Figure 14b depicts the situation when the lock gate remains open.

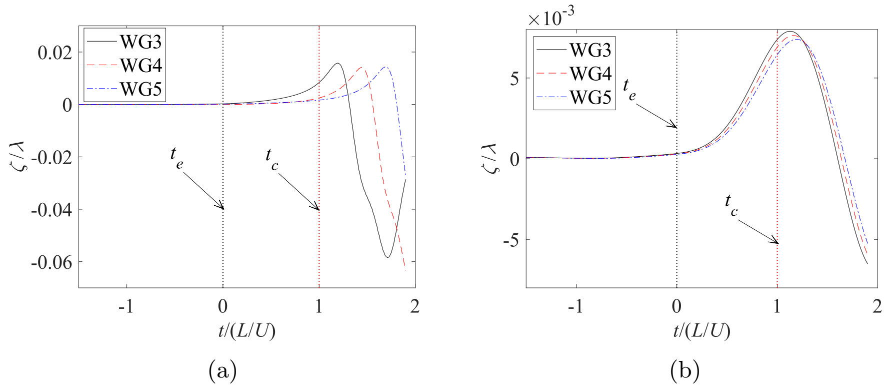

(a)

(b)

Fig. 14: Free surface elevation at WG3, WG4 and WG5: (a) the steady case; (b) the case with lock gate opened

In the scenario depicted in Figure 14b, it can be observed that the free surface at the three points begins to rise simultaneously after the ellipsoid starts to enter the lock ($t/(L/U) > 0$) and then rapidly declines shortly after the ellipsoid is fully in the lock. Initially, this phenomenon appears to align with the definition of the piston effect. However, upon closer examination, it is evident that there is a slight time difference rather than complete synchronization in the wave elevations at the three points, both when they start to rise and when they begin to decline. This discrepancy arises because the three points are in close proximity to each other, causing their movements to appear highly consistent.

To circumvent the unrealistic compression of the free surface during the lock entry process caused by an insufficiently extended calculation domain, this study significantly extended the length of the lock and conducted a new simulation with the gates kept open, as shown in Figure 15a. As depicted in Figure 15b, a significant uplift is observed on the free surface after $t/(L/U) > 0$, attributable to the inclusion of the unsteady effect in this scenario. However, these undulations no longer occur simultaneously but rather sequentially as the ellipsoid approaches. In other words, due to the unsteady effect, a long unsteady wave is generated when the ellipsoid enters the lock, and the variation of the free surface inside the lock, particularly at points distant from the lock entrance, is caused by the propagation of this long wave. It is evident that this motion differs from the piston motion. Therefore, piston motion can only be observed when the lock gate is closed. The presence of the lock gate halts the accelerated water particles from continuing to move forward. The kinetic energy is then converted into gravitational energy, which is subsequently transformed back into kinetic energy, leading to the rising and falling of the free surface as described previously.

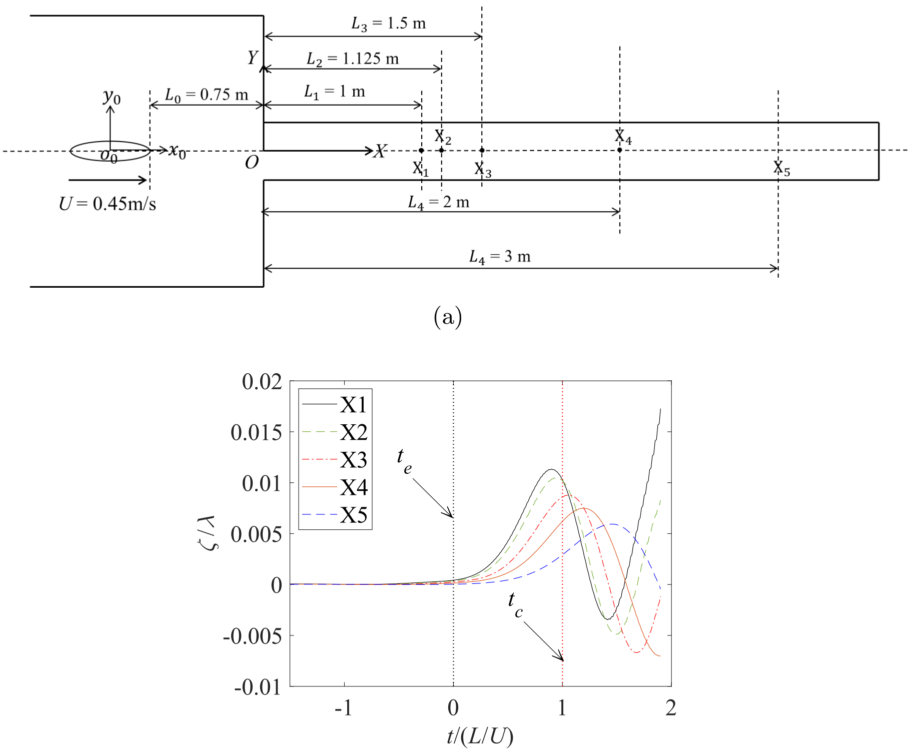

(a)

(b)

Fig. 15: The case of the lock gate being kept open: (a) positions where wave data are recorded; (b) wave cuts at the corresponding locations

Negative resistance phenomenon

It is also intriguing to observe the wave making resistance coefficient as it exhibits a negative value after the ellipsoid is fully in the lock ($t/(L/U) > 1$). This phenomenon is closely linked to the wave field around the ellipsoid. As illustrated in Figure 16a, the wave making resistance rapidly increases after the ellipsoid enters the lock, mirroring the changes in the wave field around the ellipsoid bow. Subsequently, as the wave elevation at the ellipsoid bow reaches its crest and begins to descend, the wave making resistance decreases accordingly.

However, when approximately half of the ellipsoid has entered the lock ($t/(L/U) = 0.5$), the wave field at the ellipsoid stern W_s starts to be influenced by the suddenly narrowed waterway. Consequently, the trend of W_s in Figure 16a is observed to decrease, leading to a slight increase in the pressure difference between the bow and stern of the ellipsoid. This results in the emergence of a second peak in the wave making resistance.

After $t/(L/U) > 1$, the wave elevation at the ellipsoid bow continues to decrease while the wave elevation at the stern keeps rising until it intersects with the bow waves. This indicates the presence of a low-pressure field at the ellipsoid bow due to the piston effect, while the stern exhibits a high-pressure field. This pressure differential generates additional thrust for the ellipsoid, eventually resulting in a negative value for the wave making resistance in Figure 16a. The wave field around the ellipsoid is also visually represented in Figure 16b.

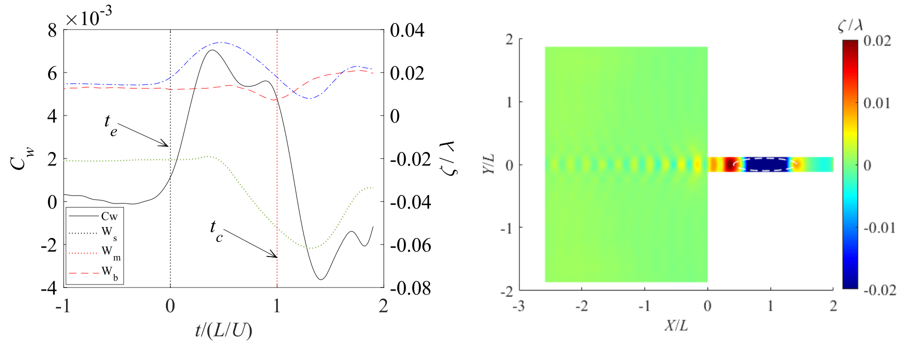

(a) (b)

Fig. 16: Free surface elevation and forces on the ellipsoid when it enters the lock at Fr=0.2: (a) wave making resistance coefficient and free surface around the ellipsoid, where W_b represents the wave elevation at ellipsoid bow, W_m shows the wave change at the middle of the ellipsoid and W_s is the wave elevation at the ellipsoid stern; (b) wave field at $t/(L/U) = 1.41$ when the ellipsoid enters the lock at Fr=0.2

A similar rationale can also be applied to elucidate intriguing findings pertaining to the heave (vertical) force. As depicted in Figure 17a, the pressure disparity between the top and bottom of the ellipsoid closely corresponds to the variation in the vertical force acting on the ellipsoid. When the ellipsoid begins to enter the ship lock, the pressure difference manifests as a negative value, indicating that the pressure at the top of the ellipsoid surpasses that at the bottom, consequently yielding a negative value for the vertical force. However, the underlying cause of this change in pressure field stems from the fluctuation in flow velocity.

After the ellipsoid enters the lock, the rising free surface within the lock draws in water, effectively propelling the water beneath the ellipsoid forward within the global coordinate system. This essentially implies a reduction in the ellipsoid's velocity, leading to a noticeable decline in F_z. Subsequently, as the piston (free surface) descends, generating a return flow at the bottom, the entry speed accelerates, resulting in an increase in the vertical force. When the free surface begins to rise again, the vertical force subsequently decreases.

The alterations in pressure around the ellipsoid offer compelling evidence for the aforementioned hypothesis. As illustrated in Figure 17b, following the commencement of the ellipsoid's entry into the lock ($t/(L/U) > 0$), there is a rapid decrease in pressure. According to Bernoulli's equation, this decrease in pressure is associated with an increase in flow velocity at the bottom of the ellipsoid, a phenomenon known as stall in the ellipsoid. Consequently, the pressure at the bottom of the ellipsoid swiftly rises, causing the flow velocity to decelerate until the free surface inside the lock reaches its maximum level, at which point the trend reverses.

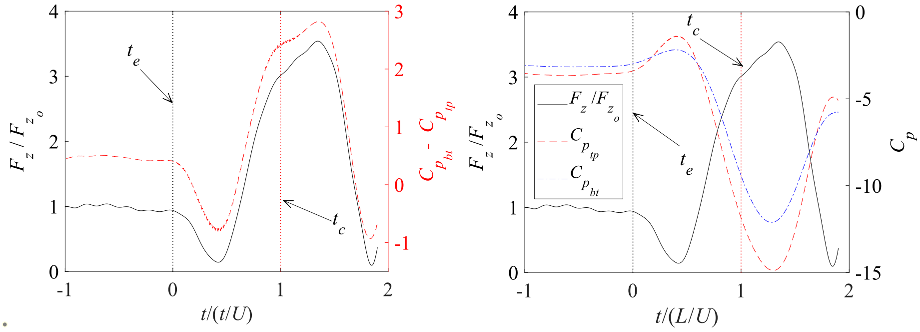

(a)

(b)

Fig. 17: Vertical force non-dimensionalized by the force at open water and the pressure acting on the the ellipsoid: (a) the pressure difference between the bottom and top surface of the ellipsoid; (b) the change of pressure around the top and bottom surface of the ellipsoid

3.2 A box entering a lock in shallow water at low speed

The insights gained from studying a submerged ellipsoid provide valuable understanding of the unsteady hydrodynamic challenges encountered during the lock entry process. However, for a more practical engineering perspective, the scenario of a ship navigating into a lock is of greater relevance. Unlike a submerged ellipsoid, a ship is a surface-piercing body, necessitating additional computational efforts to accurately model the free surface dynamics at each time step. Moreover, ships typically have widths that closely match the lock width, and the water depth is shallow. In real-world scenarios, ships enter locks at very low speeds. Given these complexities, it becomes imperative to design and conduct further model tests.

To ensure the validation and benchmarking of experimental outcomes, a straightforward and well-defined object was chosen as the prototype for these experiments. Consequently, a box-shaped object was selected as the target model.

3.2.1 Experimental set-up

The experiment was conducted in the towing tank of the Kelvin Hydrodynamics Laboratory (KHL), which boasts dimensions of 76 meters in length, 4.6 meters in width, and a maximum depth of 2.5 meters, as illustrated in Figure 18. Further comprehensive details regarding this facility can be accessed via KHL's official website.

Fig. 18: The towing tank of KHL

The Third Set of lock chambers of the Panama Canal, which have a length varying between 427m and 488m and a width of 55m[18], was chosen as the lock model.

For ease of model construction and to facilitate benchmarking against experimental data, this study selected a Bulk carrier with a block coefficient (C_B) closest to 1. This allowed for simplifying the ship hull into a box-like structure for experimentation, with a scale model built at 1/115 scale. The specific dimensions of the model box and the lock are outlined in Table 2.

Table 2: Model information

	Lock (MS)	Box (MS)
$\boldsymbol{L}$ (m)	3.5	2.4
$\boldsymbol{B}$ (m)	0.5	0.4
$\boldsymbol{T}$ (m)	0.225	0.15
$\boldsymbol{D}$ (m)	0.3	0.2

Within the test environment, water level fluctuations were measured using wave gauges positioned at five distinct locations, as depicted in Figure 19c. Specifically, the wave elevation in front of the box's bow was recorded by an ultrasonic wave probe, which moved in tandem with the box. Additionally, the waves within the lock were monitored by four fixed resistance wave gauges.

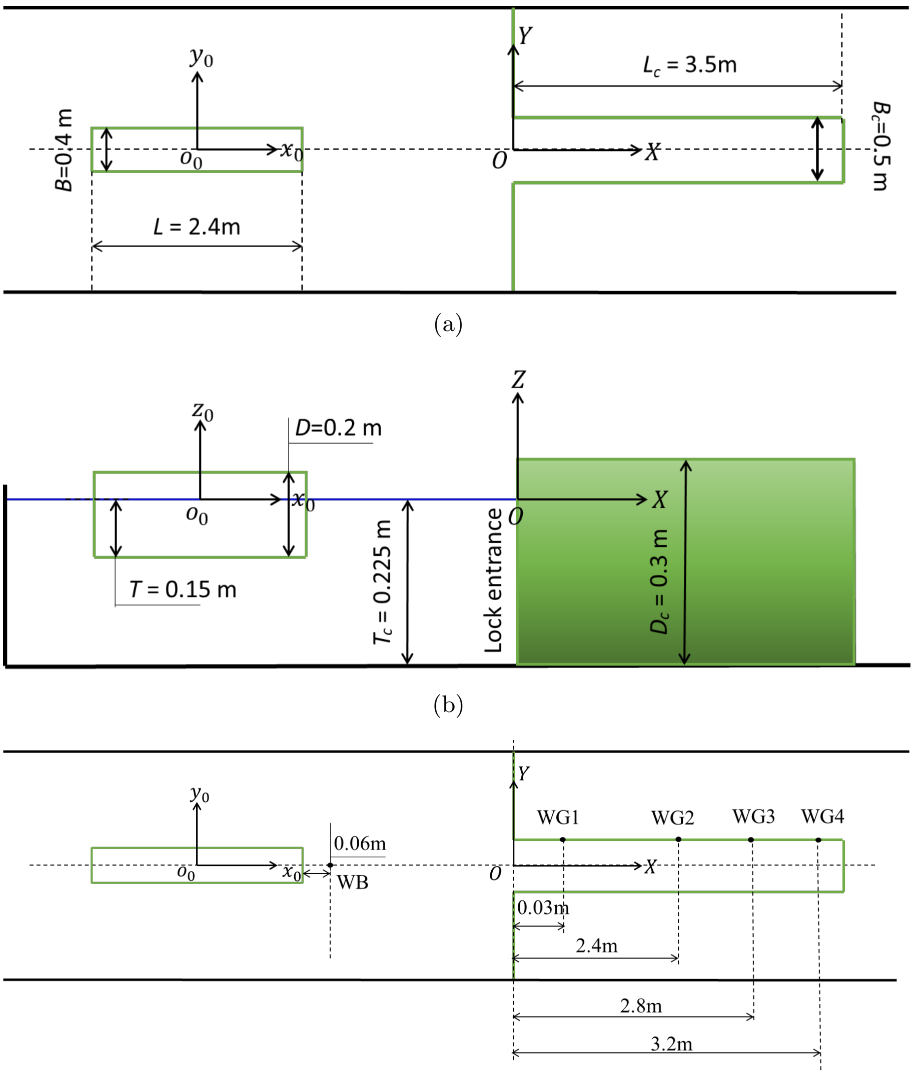

(a)

(b)

(c)

Fig. 19: General layout of the towing tank for a box entering a lock and the positions of wave gauges: (a) top view of the tank; (b) side view of the tank; (c) the positions of wave gauges

In the tests, the ship and lock model were constructed by means of marine plywood. The ship model was appropriately ballasted to ensure a watertight closure. To secure the lock model made in place, L-shaped wooden frames were affixed to its exterior, facilitating the placement of weights for stability (refer to Figure 20). The box was towed by the carriage equipped with a computer-controlled digital drive that has great speed repeatability. Meanwhile, the box model was fixed in all six degrees of freedom which means the sinkage and trim will be obtained from the force divided by the hydrostatic restoring force. At the connection point of the carriage and the box, a piezoelectric multicomponent dynamometer provided by the company called Kistler was set to capture the resistance of the box during the lock entry process. This apparatus provided measurements of sway force and yawing moment around the box's origin.

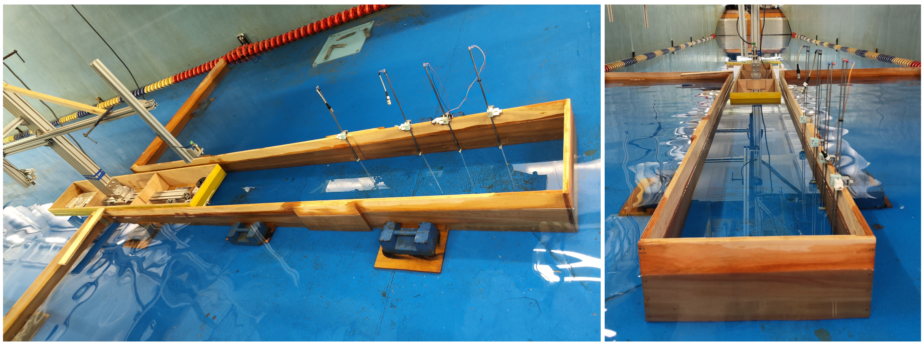

Fig. 20: Floating box entering the lock

Due to the unsteady nature of the test conditions, the reproducibility of the experiment is closely related to the acceleration phase of the box and the sudden narrowing of the channel. Especially when the box's acceleration starts at a relatively short distance from the lock entrance, the measured wave elevations inside the lock, particularly at the entrance, can be significantly affected. To avoid such a situation, the test is set to begin in calm water, and the position where acceleration starts is set at a distance of 12 meters from the entrance of the lock. This ensures that the box has enough distance to accelerate before reaching the entrance, minimizing the impact from acceleration waves.

3.2.2 Validations and discussions of the numerical simulation

The panel distribution of this case in the simulation is shown in Figure 21:

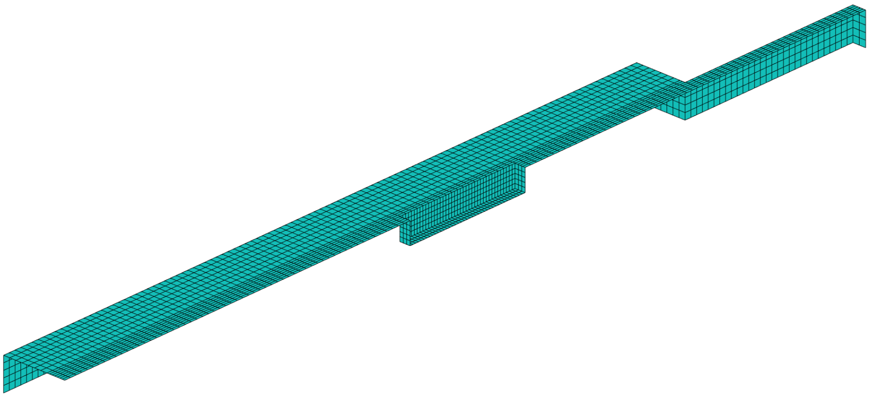

Fig. 21: Panel distribution on the computation domain of a box entering a lock model: the computational domain is truncated at $3.5L$ upstream, $1L$ sideways and $3.5L$ downstream. This study ultimately arranged 520 panels on the body surface, 2,746 panels distributed across the free surface, and 1,510 panels on the bank surface

The experiment comprised five different velocity conditions, denoted by U values of 0.1 m/s, 0.15 m/s, 0.2 m/s, 0.25 m/s, and 0.3 m/s. For the purpose of comparison, results from three sets of experiments conducted at velocities of $U = 0.1$ m/s (Fr=0.02), $U = 0.2$ m/s (Fr=0.04), and $U = 0.3$ m/s (Fr=0.06) were analysed.

As depicted in Figure 22, the total resistance acting on the box demonstrates a notable stepwise increase with increasing box velocity. This observed trend can be attributed to the influence of unsteady effects. With an increase in the box's velocity, a greater volume enters the lock per unit of time. Consequently, the channel experiences a sudden constriction, leading to a more pronounced unsteady effect. A more comprehensive analysis supporting this observation will be presented in a subsequent section.

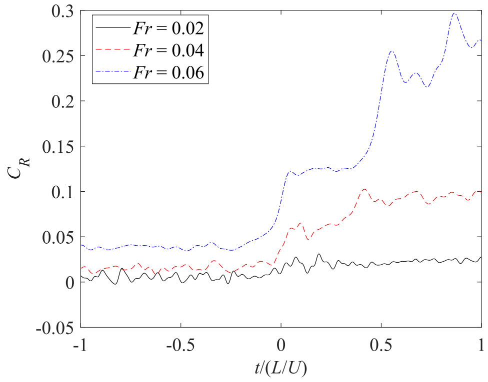

Fig. 22: Results of the model experiments at different Froude number where C_R is the dimensionless coefficient of the total resistance applied on the box: the x-axis represents both the dimensionless time and, simultaneously, the position of the bow of the box throughout the entire process of it entering the lock. When $t/(L/U) = 0$, the bow of the box has just reached the entrance of the lock

Upon comparing the waves generated by the box within the lock at different velocities (as depicted in Figure 23), it is evident that the anticipated piston effect is not pronounced at a velocity of 0.1 m/s, where the influence of viscosity on the fluid becomes prominent. As the velocity increases, a noticeable simultaneous rise in the free surface within the lock is observed, followed by sustained oscillations at the higher level. However, a simultaneous drop in the free surface is still not reflected in the experimental results. This can be attributed to the limited space between the lock banks and the sides of the box in this experiment, which restricts the fluid's ability to flow from both sides of the lock to the outside. It is anticipated that with a further increase in velocity, this constraint would alleviate.

Therefore, the model experiment conducted at a velocity of 0.3 m/s has been specifically chosen as a focal point for our case study. This deliberate selection is due to the fact that at this particular velocity, the elevation of the free surface within the lock becomes more prominent. In the subsequent sections, meticulous comparisons will be made between the numerical results obtained from MHydro, data derived from CFD simulations, and experimental observations.

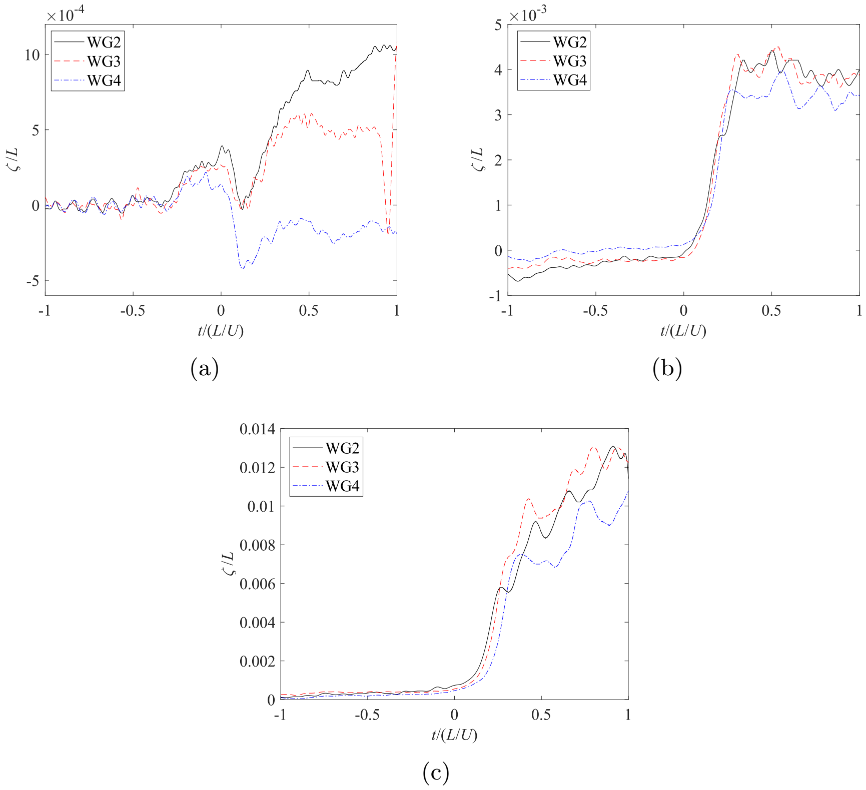

(a) (b)

(c)

Fig. 23: Wave elevations in the lock at different Froude numbers: (a) F_r=0.002; (b) F_r=0.004; (c) F_r=0.006

Validation of the numerical simulation

As depicted in Figure 24a, MHydro successfully captures the trend of the surge force variation when the box starts entering the lock. However, many fine details are still lost. In the initial stage, there is a discrepancy between the results obtained from MHydro and the experimental results. This disparity arises because MHydro can only provide the wave making resistance experienced by the box during its forward motion, whereas the experimental results account for the total resistance, including frictional forces. Particularly at this stage, with a low Froude number (Fr=0.06), indicating a very low velocity of the box, frictional resistance plays a significant role in contributing to the total resistance.

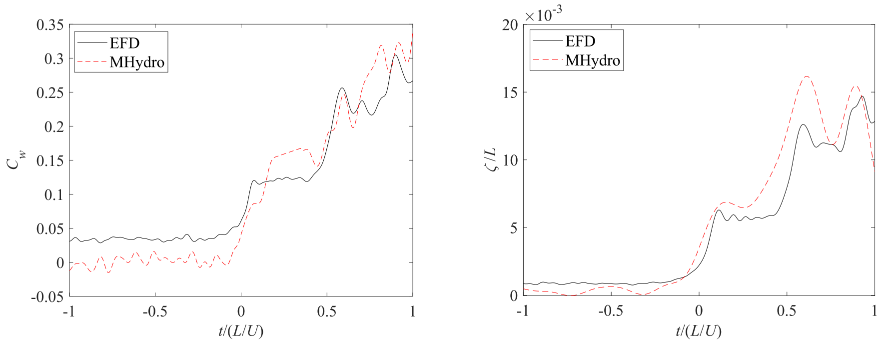

(a) (b)

Fig. 24: Comparison of the surge force applied on the box and the wave elevation at the bow while F_r=0.06 where the result from EFD is total resistance and MHydro's result is wave making resistance: (a) surge force; (b) waves at the bow

Another piece of evidence supporting this observation is presented in Figure 24b, which illustrates that MHydro reasonably captures the wave elevation at the bow of the box during the lock entry process. As depicted, the experimental results exhibit three distinct steps, occurring at $t/(L/U)$ equal to 0.2, 0.5, and 0.75. Similarly, the numerical simulation results also reflect this trend quite well, although the positions of the steps are slightly different.

Figure 25 displays the wave field within the lock during the box's entry process. From this, it can be directly observed that the elevation of the bow waves undergoes three distinct transitions, occurring approximately at $t/(L/U)$ equal to 0.1, 0.6, and 0.9.

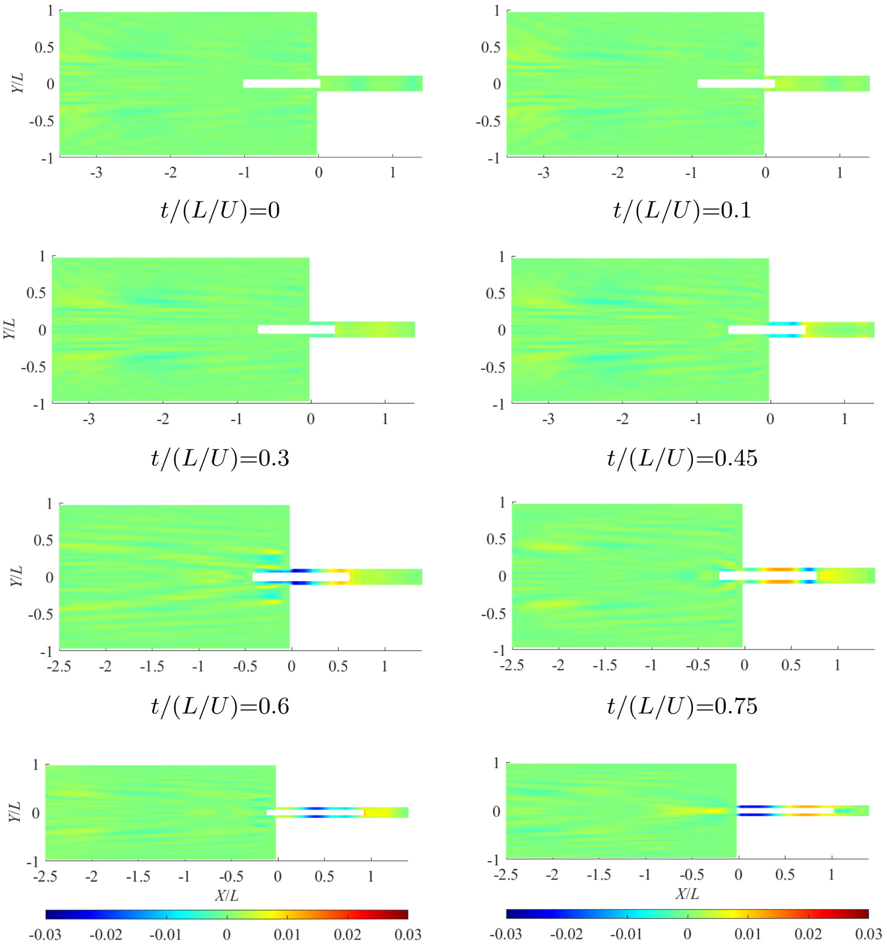

$t/(L/U)$=0

$t/(L/U)$=0.1

$t/(L/U)$=0.3

$t/(L/U)$=0.45

$t/(L/U)$=0.6

$t/(L/U)$=0.75

$t/(L/U)$=0.9

$t/(L/U)$=1

Fig. 25: The wave field in the lock when the box is entering the lock, where the color bar represents ζ/L

Figure 26 illustrates the validation of the predicted wave heights within the lock. The location of the wave gauges can be found in Figure 26e. The simulation results from MHydro generally exhibit good agreement with the experimental fluid dynamics (EFD) results. Wave elevation oscillations are also well reflected in the predictive results, although certain details remain unaccounted for. In contrast, the results obtained from computational fluid dynamics (CFD) are in excellent agreement up to $t/(L/U) \leq 0.6$. However, beyond this moment, the experimental results exhibit a stable trend, while CFD predictions continue to rise.

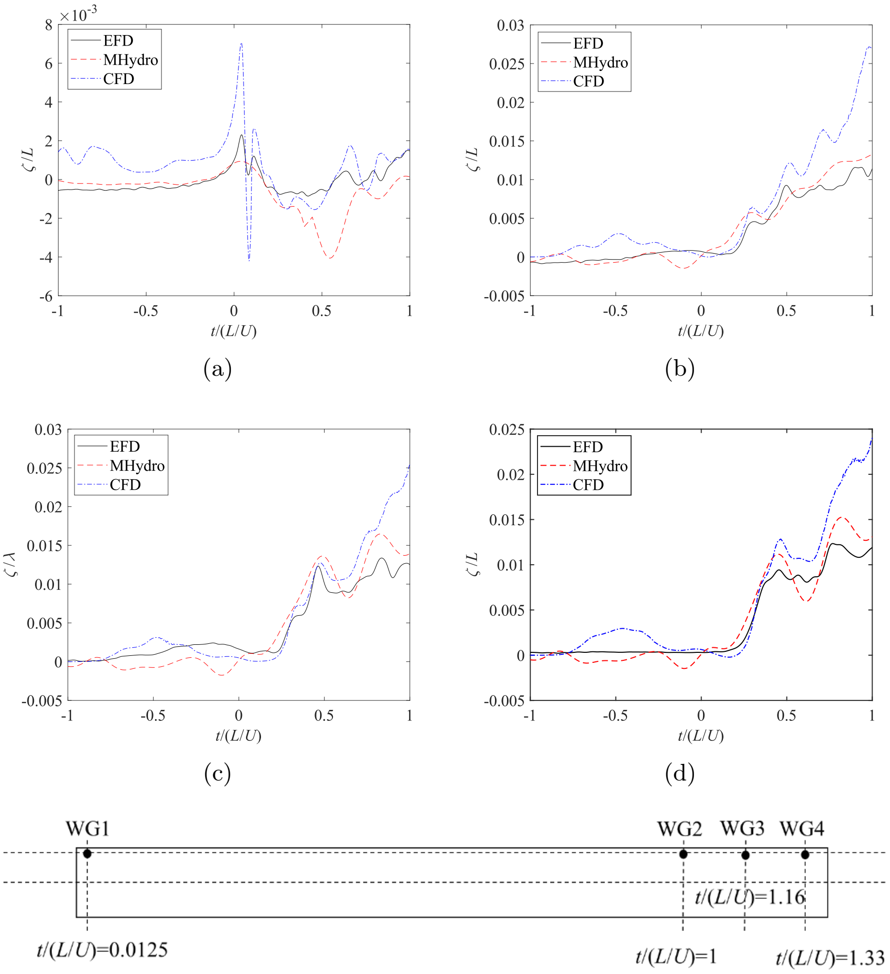

(a)

(b)

(c)

(d)

(e)

Fig. 26: Comparison of the wave elevations in the lock while F_r=0.06: (a) waves at WG1; (b) waves at WG2; (c) waves at WG3; (d) waves at WG4; (e) positions of wave gauges

It can be observed that initially, as the box just begins to enter the lock, there is a relatively small change in the volume of fluid within the lock ($t/(L/U) \leq 0.2$). Consequently, there is no significant variation in the free surface. Subsequently, as the box continues to enter, the box's kinetic energy is converted into gravitational potential energy, leading to a rapid rise in the free surface. As mentioned in the previous section, after reaching its highest level, the gravitational potential energy is reconverted into kinetic energy, resulting in the outflow of fluid from the lock and a subsequent overall decrease in the free surface. However, this phenomenon was not observed in this case.

When $t/(L/U) = 0.45$, the free surface inside the lock reaches its highest level and then continues to oscillate at that location. This indicates that at this moment, the kinetic energy absorbed and lost by the fluid has reached a balance, so the height of the free surface no longer shows significant changes.

Return flow phenomenon

Although the box sails along the positive x-direction with a constant speed U, once it reaches the entrance of the lock, the water volume will increase due to the sudden narrowing of the waterway. This increase in volume elevates the free surface height within the lock and induces significant return flow inside the lock. This return flow has a substantial impact on the results. In the present study, the effect of return flow will be incorporated into the body surface boundary condition. The increased volume can be expressed as:

$$\Delta V = U A_s(t) \cdot \Delta t \tag{16}$$

where A_s is the cross-section area of the box's wetted surface at moment t. This means a return flow will follow and the same volume of water will flow through the clearance between the ship and the lock bank. As the box keeps entering the lock, the distance between the bow of the box and the lock gate will continue to decrease which results in an increase of the return flow velocity $v(x,\, t)$ [12]. Considering the return flow as a uniform flow, the effect of the return flow can be treated as an additional time-dependent velocity term on body surface boundary condition $v(t)$:

$$\frac{\partial \varphi}{\partial n} = [U + v(t)] n_1 \tag{17}$$

where $v(t)$ can be obtained by:

$$v(t) = \begin{cases} 0, & \text{while } t \leq t_e \\ \kappa \frac{\delta}{l} \left(t - t_e\right) U^2, & \text{while } t_e < t \leq t_c \end{cases} \tag{18}$$

where δ is the blockage ratio which equals the ratio of the cross-section area of the box to that of the lock, l is the lock length, t_e represents the moment when the box arrives at the entrance of the lock and t_c represents the moment when the ship is totally in the lock. As the existence of the return flow, the box will receive an acceleration and κ is, therefore, the acceleration coefficient. After the moment t_c, the return will still exist. However, the acceleration coefficient will be smaller than κ because the total water volume in the lock will remain constant at this time, while the return flow mainly comes from the change in water volume. In this case, an empirical iteration method is introduced to estimate the return flow velocity:

$$v\left(t_n\right) = v\left(t_{n-1}\right) + \kappa \frac{\delta}{l} (U \Delta t) \left[v\left(t_{n-1}\right) - v\left(t_c\right) + U\right], \text{ at } t > t_c \tag{19}$$

where $v(t)$=$v(t_c)$ is the initial condition of Eq. (19).

As shown in Figure 27, most of the hydrodynamic phenomena within the lock are primarily attributed to the presence of return flow. When the return flow is not considered in the simulation (κ=0), there is almost no noticeable change in the free surface within the lock. However, wave resistance is closely related to the wave elevations, and as a result, the prediction of wave making resistance is completely distorted under this condition. Through comparison with experimental results, this study found that when κ=15, the simulation results align quite well with the experimental data. This represents a compromise as the determination of the coefficient is closely related to specific factors such as hull shape.

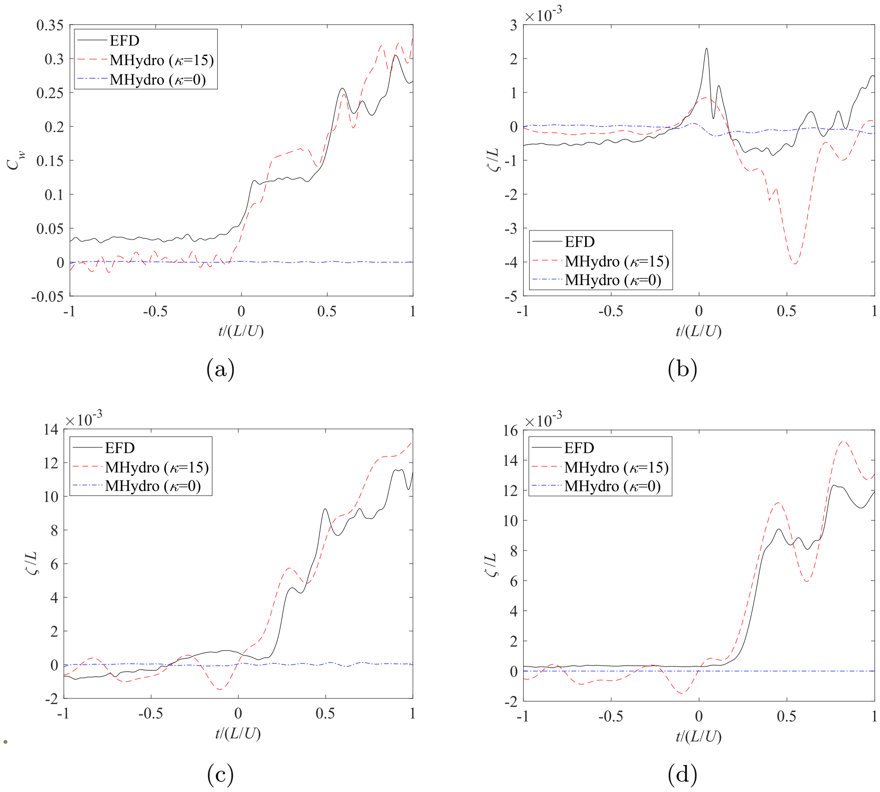

(a)

(b)

(c)

(d)

Fig. 27: Comparison of the numerical simulation results with different acceleration coefficient κ while F_r=0.06: (a) wave making resistance; (b) waves at WG1; (c) waves at WG2; (d) waves at WG4

Finally, this study revealed that the return flow within the lock is non-uniform. Fluid near the bow of the box experiences more pronounced effects of return flow compared to positions closer to the banks. This disparity can be attributed to the box's entry, which initiates the return flow phenomenon. Consequently, the flow field around the bow, moving in conjunction with the box, naturally exhibits a stronger correlation with the return flow compared to fixed positions located farther from the box.

Free surface effect and piston phenomenon

Figure 28 presents a comparison of the total resistance and wave making resistance obtained using different methods, where the experimental results from EFD provide the total resistance C_R, while the results from MHydro only include the wave making resistance C_w. It can be observed that the numerical simulation results progressively converge towards the experimental results, beginning from treating the free surface as a rigid wall, then establishing a linear quasi-steady free surface, and finally incorporating unsteady effects on the free surface. Remarkably, the step phenomena observed in the experimental results are only replicated in the fully unsteady simulation results, indicating a close association with unsteady effects. This elucidates why the step phenomena become more pronounced only as the box's velocity increases. A higher entry velocity induces more significant unsteady effects on the free surface within the lock. Figure 29 further underscores the necessity of establishing a 3D free surface and considering its unsteadiness in the current problem.

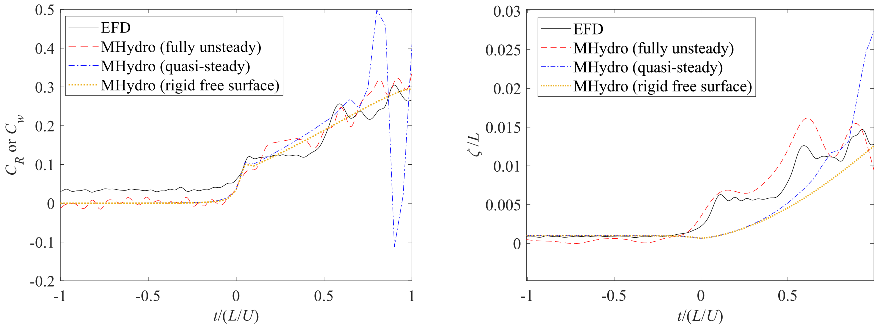

(a) (b)

Fig. 28: Resistance applied on the box obtained by different methods: (a) surge force; (b) waves at the bow

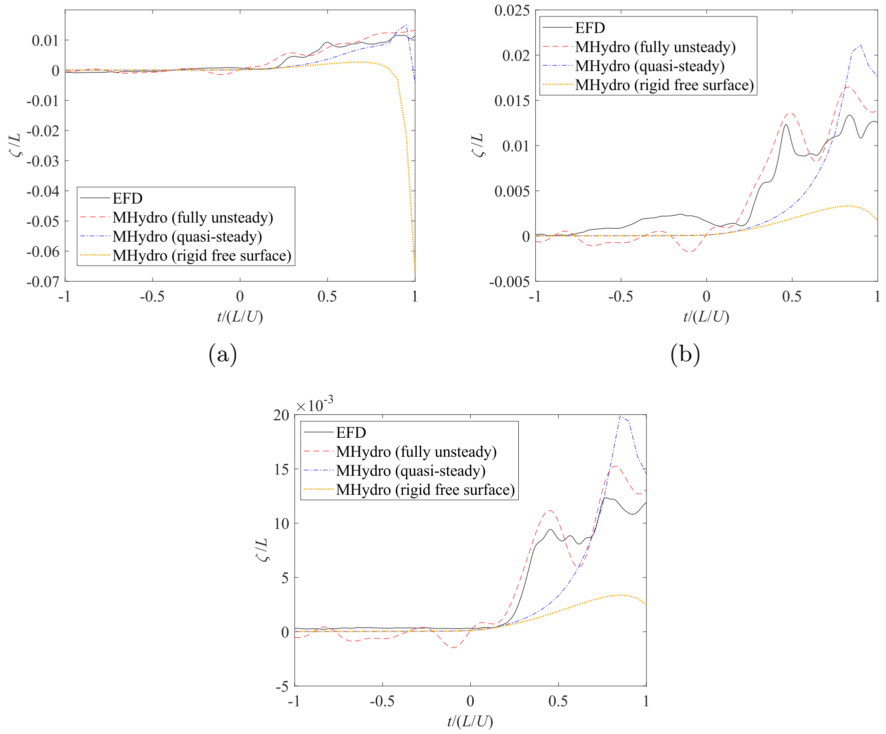

(a)

(b)

(c)

Fig. 29: Wave elevations inside the lock: (a) waves at WG2; (b) waves at WG3; (c) waves at WG4

Furthermore, this study reveals that the unsteady effects of the free surface are indispensable for simulating the piston phenomenon inside the lock. When the free surface effects are completely disregarded, the free surface inside the lock only rises sequentially as the bow of the ship approaches, influenced by the high-pressure field. However, when a linear quasi-steady free surface is established, although the free surface inside the lock can also rise simultaneously, the entire process follows a smooth curve rather than the abrupt lift observed in the experiments as the box enters. Only the results obtained using the fully unsteady MHydro method effectively replicate this phenomenon, as shown in Figure 30.

However, as previously mentioned, the free surface level did not exhibit a clear simultaneous decrease phenomenon in the current case. Nevertheless, some trends resembling simultaneous decreases can still be observed in the changes of waves at WG3 and WG4. As shown in Figure 30a and Figure 30d, from $t/(L/U) = 0.5$ to $t/(L/U) = 0.8$, the wave elevations at both locations underwent a process of initial decrease followed by an increase, and this change occurred simultaneously. The reason for this phenomenon lies in the energy, as previously explained. Additionally, from an external perspective, it is also due to the relatively larger flow space at these two points, as they are farther from the lock entrance, enabling the lowering of the free surface.

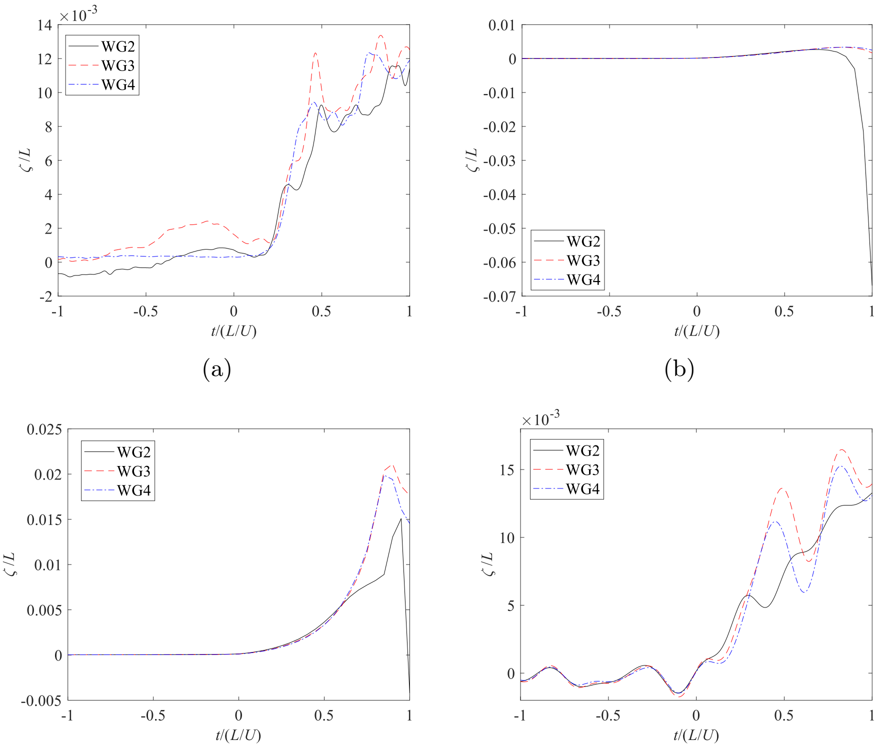

(a) (b)

(c) (d)

Fig. 30: Wave elevations at WG2, WG3 and WG4: (a) EFD results; (b) results with a rigid free surface; (c) results with a quasi-stady free surface; (d) results with a fully unsteady free surface

3.3 Summary

This chapter delves deeply into the physical phenomena occurring during the entry of an object into a narrow waterway, as evidenced through two distinct case studies. Initially, the examination uncovers a notable piston-like motion of the free surface within the lock. However, this finding is qualified by the utilization of a fully submerged ellipsoid with relatively high velocity and deep water conditions, leading to discernible deviations from real-world scenarios. Subsequently, a second case study is introduced to address these discrepancies. Here, stringent constraints are imposed on water depth and lock width, resulting in a box cross-sectional area approaching that of the lock.

Additionally, the ship's entry speed is regulated to better align the simulation with actual ship-lock entry scenarios.

In the first case study, the observation of piston-like motion of the free surface inside the lock is highlighted, whereas the second case study reveals significant return flow phenomena within the lock, exerting a notable influence on the hydrodynamics of the box. Thus, while the piston-like phenomenon primarily correlates with the object's speed, the return flow phenomenon is intricately linked to the object's shape and the ratio of cross-sectional areas between the object and the lock.

4 Conclusion

The current study delves into the numerical and experimental exploration of unsteady hydrodynamic phenomena occurring when a moving body enters a lock. Through meticulous investigation, the study unveils a piston phenomenon characterized by periodic rises and falls of the free surface as an ellipsoid enters a lock. This phenomenon is intricately linked to the unsteady effects induced by the sudden narrowing of the channel and the closure of the lock gate. Moreover, the study elucidates that the intensity of the piston effect is closely tied to the speed of the ellipsoid; higher speeds accentuate the significance of unsteady effects, thereby amplifying the piston effect. Additionally, the study uncovers the occurrence of negative resistance, attributed to the rising free surface at the ellipsoid's front, subsequently creating a low-pressure field within the lock, compelling the ellipsoid to move towards it, resulting in negative wave making resistance.

Furthermore, by simulating and comparing the entry of a box into a narrow lock at low speeds, the study demonstrates that the potential flow solver MHydro generally captures the forces acting on the box and the trends of wave generation during lock entry. However, it acknowledges limitations in fully capturing all intricacies of flow dynamics, attributing these shortcomings to the simplifications in the return flow model utilized. The non-uniform nature of return flow within the lock introduces inaccuracies in simulation results, necessitating future efforts to enhance prediction models.

Finally, while a pronounced piston effect was not observed during the entry of the box into the lock due to constraints imposed by the narrow gap between the box, lock walls, and bottom, the study emphasizes that the absence of this phenomenon in this specific case does not negate its existence during ship-lock interactions. The occurrence and magnitude of the piston effect are intricately linked to the ratio of the cross-sectional area of the ship to that of the lock, as well as entry velocity, warranting further research to comprehensively understand its influence.

References

[1] Vantorre, M., Richter, J.: Maneuverability in lock access channels. In: "What's New in the Design of Navigation Locks" 2nd International Workshop, PIANC–New Orleans, vol. 2 (2011)

[2] Schoenherr, K.: Data for estimating bank suction effects in restricted water and on merchant ship hulls. In: First Symposium on Ship Maneuverability, pp. 199–210 (1960)

[3] Norrbin, N.H.: Bank effects on a ship moving through a short dredged channel. *Naval Hydrodynamics Series* (1976)

[4] Lataire, E., Vantorre, M., Delefortrie, G.: Captive model testing for ship to ship operations. In: International Conference on Marine Simulation and Ship Maneuverability (2009)

[5] Lataire, E., Delefortrie, G., Vantorre, M.: Impact of banks on ship squat. In: 4th International Conference on Ship Manoeuvring in Shallow and Confined Water, pp. 115–121 (2016)

[6] Lataire, E., Vantorre, M., Delefortrie, G.: A prediction method for squat in restricted and unrestricted rectangular fairways. *Ocean Engineering* **55**, 71–80 (2012)

[7] Lataire, E., Vantorre, M., Delefortrie, G., Candries, M.: Mathematical modelling of forces acting on ships during lightering operations. *Ocean Engineering* **55**, 101–115 (2012)

[8] Vantorre, M., Verzhbitskaya, E., Laforce, E.: Model test based formulations of ship-ship interaction forces. *Ship Technology Research* **49**, 124–141 (2002)

[9] Vrijburcht, A.: Calculations of wave height and ship speed when entering a lock. Technical report (1988)

[10] Meng, Q., Wan, D.: Urans simulations of complex flows around a ship entering a lock with different speeds. *International Journal of Offshore and Polar Engineering* **26**(02), 161–168 (2016)

[11] Wan, Z., Li, Y., Wang, X., An, J., Cheng, L., Liao, Y.: Effect of ship-lock-induced surges on navigation safety in a branched lower approach channel system. *Journal of Hydroinformatics* **24**(2), 481–496 (2022)

[12] Yuan, Z.M.: Ship hydrodynamics in confined waterways. *Journal of Ship Research* **63**(01), 16–29 (2019)

[13] Terziev, M., Liu, Y., Yuan, Z., Incecik, A.: The resistance of a trans-critically accelerating ship in shallow water. *Ship Technology Research* **71**(1), 14–32 (2024)

[14] Li, M., Yuan, Z.M., Yeung, R.W.: Unsteady wave-making resistance of an accelerating ship. In: International Conference on Offshore Mechanics and Arctic Engineering, vol. 84379 (2020)

[15] Kozin, V., Zemlyak, V.: Study on wave resistance of a submarine moving under

an ice sheet. In: ISOPE International Ocean and Polar Engineering Conference, pp. 1312–1314 (2012)

[16] Terziev, M., Tezdogan, T., Incecik, A.: Application of eddy-viscosity turbulence models to problems in ship hydrodynamics. *Ships and Offshore Structures* **15**(5), 511–534 (2020)

[17] Terziev, M., Tezdogan, T., Incecik, A.: Scale effects and full-scale ship hydrodynamics: A review. *Ocean Engineering* **245**, 110496 (2022)

[18] Delefortrie, G., Willems, M., Vantorre, M., Laforce, E.: Behavior of post panamax vessels in the third set of panama locks. In: International Conference on Marine Simulation and Ship Maneuverability (2009)